Hierarchically structural layered double oxides with stretchable nanopores for highly effective removal of protein-bound uremic toxins

Siping Ding, Dong Wang, Xuefen Wang [*]

State Key Laboratory for Modification of Chemical Fibers and Polymer Materials, College of Materials Science and Engineering, Donghua University, Shanghai 201620, PR China

ARTICLE INFO

ABSTRACT

The global outbreak and prevalence of coronavirus disease 2019 (COVID-19) has triggered an urgent demand for family hemodialysis equipment. It is particularly vital to design and apply superior adsorbents to adsorb toxins for reducing the usage of dialysate. In this work, hierarchically structural MgAl layered double oxides (LDO) with stretchable nanopores were exploited through a facile one-pot trisodium citrate (TSC) assistant hydrothermal reaction followed by calcination treatment for effectively adsorbing protein-bound uremic toxins such as hippuric acid (HA) or indoxyl sulfate (IS). The optimized MgAl LDO possessed flower-like spherical morphology, ultrahigh specific surface area (187.3 m^2/g) and uniquely stretchable nanopores, which were more conducive to incorporating anions due to their unique memory effect endowing them with promising adsorption capacities for HA or IS. And the adsorption data could be better conformed to pseudo-second-order kinetic model and Langmuir isotherm determining that the maximum adsorption capacity of HA and IS was 129.8 mg/g and 63.1 mg/g, respectively. Furthermore, the computation of molecular size paired with the analysis of adsorption mechanism accurately revealed that high-efficiency toxin capture was mainly attributed to electrostatic interaction for internal intercalation and surface adsorption. Therefore, the application of such delicate LDO as new premium adsorbent would facilitate the development and popularization of family hemodialysis equipment.

1. Introduction

Globally, kidney diseases were impacting the lives of roughly 850 million people and over 5 million patients died each year due to lack of timely and appropriate treatment [1,2]. Unfortunately, the rampant COVID-19 as a complex multisystem syndrome was implicated in function abnormalities of multiple organs, which would further exacerbate kidney impairment particularly [3,4]. Patients commonly required hemodialysis to eliminate the accumulation of various uremic toxins including water-soluble small-molecular toxins, middle-molecular toxins and protein-bound uremic toxins (PBUTs) from the blood for therapy [5–7]. However, conventional hemodialysis was offered three times weekly and demanded significant volumes of costly dialysate, which heavily limited the miniaturization and portability of hemodialysis device [8,9]. Especially, with the continued global spread of COVID-19, attending to specialized facilities for dialysis treatment not only imposed a burden on the prevention and control of the epidemic, but also increased the infection risk for patients and medical staff rendering the development of home-based dialysis systems become

more pressing in quarantine [10,11]. As a result, it was critical to miniaturize the hemodialysis device to enable family dialysis convenient and economical.

With the development of portable artificial kidneys (PAK), different adsorbents layers were placed in the dialysate to adsorb various uremic toxins for continuously keeping the free toxin concentration at low level and dialysis driving force at high altitude, which had become an effective way to substitute vast quantities of dialysate [9,12]. Among the various toxins, PBUTs such as IS and HA were relatively special type of toxins with two different typical forms, of which one was conjugated to important protein and the other was free toxin in blood [13]. There was a dissociative equilibrium between the two forms of toxin suggesting that the equilibrium shifted towards dissociation of the complex prompting the release of more free toxins when part of free toxin was eliminated [13,14]. In this regard, to achieve efficient removal of PBUTs, the concentration of free toxins in the dialysate must be low so that the free fraction in the plasma could diffuse rapidly into the dialysate, which also promoted a shift in equilibrium to dissociation facilitating the continued release of toxin bounded to protein into the plasma

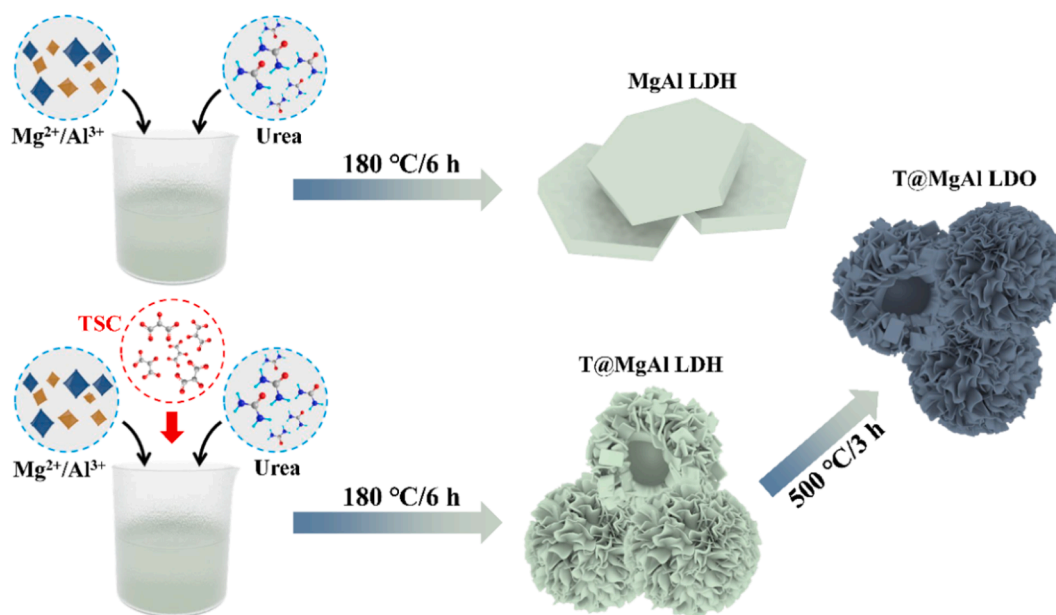**Scheme 1.** Schematic diagram of the preparation procedure of bulky MgAl LDH, flower-like T@MgAl LDH and T@MgAl LDO.

and then further penetrated into dialysate [14,15]. Indeed, the introduction of effective adsorbents targeting PBUTs in dialysate not only enhanced the clearance of PBUTs from blood, but also followed and expanded the route of PAK development. Recently, Li et al. proposed that using cyclodextrin-based polymers to adsorb toxins from dialysate could enhance the clearance of PBUTs, but the adsorbent had cumbersome preparation process and tend to dissolve [16,17]. Moreover, in our group, we put forward the concept of lightweight hemodialysis and reduced the usage of the dialysate to one tenth of its original volume by introducing toxin adsorbent with small amount whatever in weight or in volume (almost negligible *vs* the amount of the dialysate) into the dialysate [9,18]. And we had also attempted to achieve effective clearance of IS by hemodialysis through the design of reduced graphene oxide (rGO) aerogels combined with thin-film nanofibrous composite membrane while the adsorption capacity for PBUTs remained to be improved [13]. Consequently, it was desirable, but challenged to design and develop an easily prepared, highly efficient and low-cost adsorbent for PUBTs.

Concerning potential adsorbent materials or precursors, LDH as a typical anion clay possessed unique structure consisting of positively charged brucite-like layers and intercalated anions [19]. Specifically, the metal layers hold a positive charge due to the fractional isomeric substitution of divalent with trivalent cations while the intercalated anions and water molecule would compensate for excess positive charge and provide hydrogen bonding between the layers, respectively [20]. As a result of this, LDH and its derivatives hold unique physicochemical properties including simple synthesis, versatile components and structure, great surface adsorption capacity and strong anion exchange performance allowing them to be widely explored and employed in various fields of catalysis, adsorption and energy storage [21–24]. On the one hand, some researchers had synthesized different LDH with distinct layer spacing and variable morphology by adding different anions to the reaction system, which had contributed to improvements in adsorption performance [25–28]. On the other hand, LDO as a calcined derivative of LDH was also a promising candidate for adsorbent with normally composed of mixed metal oxides or spinel [29]. And the calcination would allow the majority of the water molecules and anions in the LDH layer to be evaporated or decomposed, which could facilitate the enhancement of surface defects and internal reactions [30,31]. Interestingly, LDO exhibited a fascinating property known as the memory effect implying that it tended to reconstruct its original lamellar

structure by spontaneous rehydration and simultaneous capture anions into the interlayer in aqueous media [32,33]. Consequently, LDO demonstrated larger specific surface area and superior anion capture performance compared to LDH making it proficiently remove organic and inorganic contaminants in wastewater, such as Cr (VI), U(VI), phosphate, and anionic dyes [19,31,34–36]. However, there were no studies on the application of LDO for the PBUTs adsorption, in spite of the fact that many advantages associated with LDO distinguished it as an idea toxin adsorbent.

Based on the above summary and inspiration, a hierarchically structural flower-like T@MgAl LDH was prepared by a facile one-pot hydrothermal reaction using Mg^{2+} and Al^{3+} as metal sources and citrate as an anionic additive. Evidently, the specific surface area of T@MgAl LDH was much higher than that of conventional bulky MgAl LDH without citrate. And then, the optimized T@MgAl LDH was converted to T@MgAl LDO by calcination maintaining its original morphology entirely, as shown in Scheme 1. Interestingly, T@MgAl LDO was evidenced to possess stretchable nanopores and exhibit great adsorption capacities for PBUTs due to internal intercalation effect and surface adsorption summarized by the calculation of molecular size combined with the analysis of adsorption mechanism. Taken together, flower-like MgAl LDO nanomaterial with hierarchical structure and stretchable nanopores was expected to be a promising candidate adsorbent towards PBUTs from dialysate for the development of family hemodialysis systems and portable artificial kidney.

2. Experimental section

2.1. Materials

Trisodium citrate ($Na_3C_6H_5O_7\cdot2H_2O$), $Al(NO_3)_3\cdot9H_2O$, $Mg(NO_3)_2\cdot6H_2O$, urea, potassium bromide (KBr), sodium oxalate and sodium gluconate were obtained from Sinopharm Chemical Reagent Co., ltd. Indoxyl sulfate potassium salt (IS) and hippuric acid (HA) were purchased by Sigma Aldrich. Deionized (DI) water was used throughout the whole experiments process. All reagents were used as received with no further purification.

2.2. Preparation of LDH and LDO

MgAl LDH was prepared through one-pot hydrothermal reaction

Sample	Al^{3+} (mmol)	Mg^{2+} (mmol)	urea (mmol)	TSC (mmol)
MA	4	4	12	0
T1@MA	4	4	12	0.4
T2@MA	4	4	12	0.8
T3@MA	4	4	12	1.2
T4@MA	4	4	12	1.6

described in the literature with slight modification [37]. Firstly, Al $(NO_3)_3 \cdot 9H_2O$, $Mg(NO_3)_2 \cdot 6H_2O$ and urea were fully dissolved in DI water. And then, different amounts of TSC were added to the solution and stirred thoroughly for 1 h. Finally, the mixture was transferred into a 100 ml autoclave with Teflon-lined and heated at 180℃ for 6 h. The resultant products were obtained by centrifugated at 8000 rpm for 5 min when the reaction was completed and cooled. The specific composition ratios and product sample names were shown in Table 1. Moreover, based on subsequent characterization, the T3@MA was chosen to be a paradigm and calcined at 500℃ for 3 h in muffle furnace to prepare MgAl-LDO labeled as CT3@MA.

2.3. Adsorption experiment

To verify that CT3@MA had a memory effect with stretchable nanopores, it was subjected to adsorption experiments for different sized anions. In detail, 40 mg of CT3@MA were dispersed in 0.1 M solutions of KBr, sodium oxalate and sodium gluconate with beaker, respectively. The beaker was fixed on thermostatic shaker at 100 rpm for 24 h. And the temperature was kept at 25℃. After the adsorption was completed, CT3@MA was removed by centrifugation and the crystalline spacing was calculated by a series of characterization. The samples were labeled as Br-CT3@MA, Ox-CT3@MA and Gl-CT3@MA, respectively.

In order to explore the adsorption behavior of CT3@MA for PBUTs, IS and HA were used as example toxin adsorbates for the following experiments. To concretely describe the adsorption equilibrium of PBUTs on CT3@MA, 5 mg CT3@MA was put in 50 ml PBUTs aqueous solution in a beaker, respectively. The beaker fixed on thermostatic shaker at 100 rpm for 24 h. And the temperature was kept at 25℃. The initial concentration range for PBUTs was 50–400 mg/L. After adsorption was completed, the concentration of the remaining solution was determined with ultraviolet (UV) spectrophotometer and calculated according to standard curves. The UV absorbance wavelength of IS and HA were 278 nm and 229 nm, respectively. The amount of toxin captured by

CT3@MA would be estimated by the difference in concentration of the toxin solution before and after adsorption. And the absorption capacity was presented in q_e (mg/g) depending on the equation (1):

$$q_e = (C_0 - C_e) \times V/W \tag{1}$$

where C_0 was the initial concentration of PBUTs (mg/L) and C_e was the equilibrium concentration of PBUTs (mg/L). V (L) was the volume of PBUTs solution and W (g) was the mass of CT3@MA.

The Langmuir and Freundlich isotherm model were defined by following equation (2) and (3) [38]:

$$\frac{C_e}{q_e} = \frac{C_e}{q_0} + \frac{1}{bq_0} \tag{2}$$

$$\ln q_e = \ln K_F + \frac{1}{n} \ln C_e \tag{3}$$

where q_e (mg/g) and C_e (mg/L) was the adsorption capacity and concentration of PBUTs residual solution at adsorption equilibrium. The q_0 (mg/g) was the maximum adsorption capacity. In addition, b (L/mg) expressed the Langmuir constant relevant to adsorption enthalpy. K_F (mg/g) as an empirical constant of Freundlich was adsorption capacity determined by the bond strength and $1/n$ reflected the surface homogeneity and capture strength.

To study the kinetic adsorption of PBUTs on CT3@MA, 50 mg CT3@MA was soaked in 500 ml PBUTs aqueous solution (300 mg/L) in beaker, which was also placed in a thermostatic shaker at 100 rpm for different time (0–300 min). And the temperature was kept at 25℃. Within the time period given, the concentration of the solution was determined with UV spectrophotometer and calculated according to standard curves. Thus, the adsorption capacity would be confirmed from variation in concentration at different time.

The adsorption kinetics could be elaborated using the pseudo-first-order and the pseudo-second-order kinetic models. And the two kinetics were expressed by two equations (4) and (5) [39]:

$$\ln(q_e - q_t) = \ln q_e - k_1 t \tag{4}$$

$$\frac{t}{q_t} = \frac{1}{k_2 q_e^2} + \frac{t}{q_e} \tag{5}$$

where q_e (mg/g) was the equilibrium adsorption capacity, and q_t (mg/g) was the capacity at the given time t (min). The k_1 (h^{-1}) and k_2 (g/mg·h) were relevant parameters in the models.
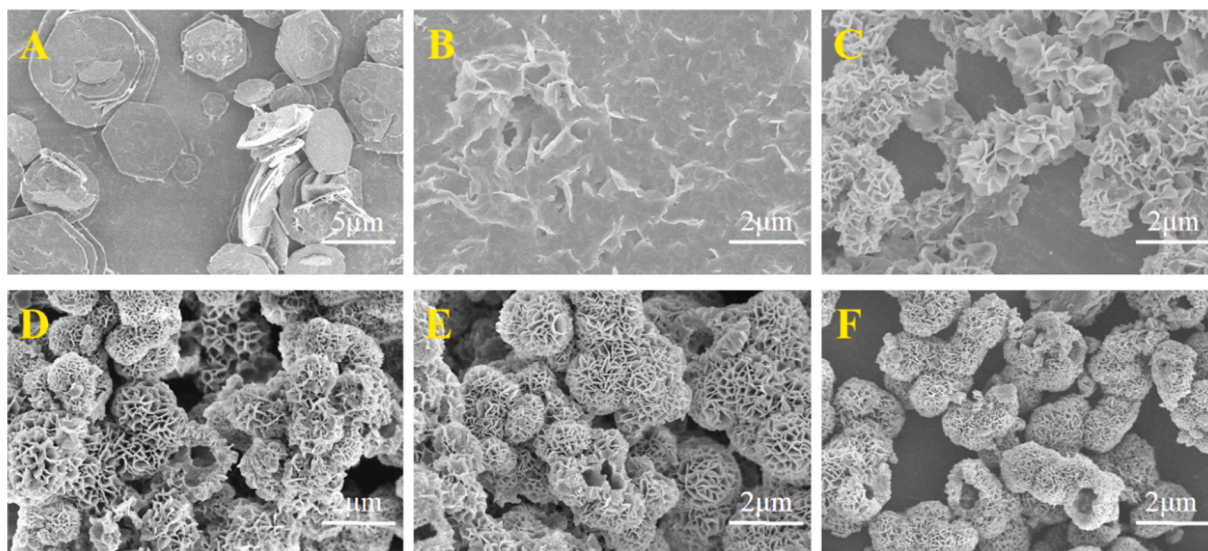

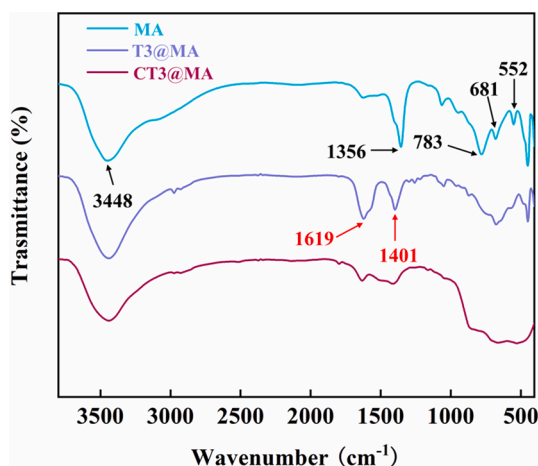**Fig. 1.** The FE-SEM images of MA (A), T1@MA (B), T2@MA (C), T3@MA (D), T4@MA (E) and CT3@MA (F).

Fig 2. The FT-IR spectrum of MA, T3@MA and CT3@MA.

2.4. Characterization

The crystalline phases of all samples in the experiment were characterized by X-ray diffraction (XRD) analyses. The surface morphologies of all samples were observed using field emission scanning electron microscopy (FE-SEM, SU8000, Hitachi, Japan). The chemical composition of the selected LDH and LDO samples were characterized by attenuated total reflectance fourier transform infrared spectra (ATR-FT-IR, Nicolet-8700, Thermometer, USA) and X-ray photoelectron spectroscopy (XPS, Kratos Analytical-A Shimadzu Group Company, Japan). The Brunauer-Emmett-Teller (BET) specific surface area of the selected LDH and LDO samples were obtained by using N_2 adsorption–desorption isotherms rely on a specific surface area analyzer (ASAP 2020, Micromeritics Co., USA). The molecular structure and size calculation were provided by Chem 3D combined with Multiwfn where the subfunction 21 of main function 100 was used [40]. The absorbance of the solution of HA or IS was determined by UV–vis spectrophotometer (TU-1950, Purkinje, China).

3. Results and discussion

3.1. Characterization of LDH and LDO

3.1.1. Morphology and composition characterization

Under high temperature conditions, Mg^{2+} and Al^{3+} were formed into MgAl LDH by hydrothermal reaction. The introduction of citrate into the system would lead to interesting changes in the morphology of the product after reaction, and the effect of adding amounts of TSC on the morphology was investigated in detail. As could be seen in Fig. 1A-B, the resultant LDH presented a typical large thick micro-sheet with uneven size without citrate, which would transform into a curled and three-dimensional lamellar structure in the presence of citrate. Moreover, as the amount of citrate increased, the nanoplate became smaller and more well-defined, eventually emerging in stacks (Fig. 1C) and assuming a complete flower-like spherical shape with delicate hierarchically structure (Fig. 1D-E). As T4@MA and T3@MA were extremely similar in morphology, T3@MA was chosen for the subsequent study. Thus, after calcination at 500℃, it was converted to LDO and the morphology remained as a flower-like sphere with a slight increase in dispersion, as shown in Fig. 1F.

To confirm the introduction and removal of citrate, the FT-IR spectrum of MA, T3@MA and CT3@MA was demonstrated in Fig. 2. The characteristic peak at 3448 cm^{-1} was the stretching vibration of –OH attributed to interlayer water molecules and LDH layer (H-OH and Mg/Al-OH) [41,42]. In particular, the characteristic peak at 1356 cm^{-1} was ascribed to the C—O groups of CO_3^{2-} in interlayer [31]. And the bands observed from 500 to 800 cm^{-1} were assignable to the vibrations of Mg-O/Al-O [43]. For T3@MA, the obvious two peaks at 1619 cm^{-1} and 1401 cm^{-1} belonged to the asymmetric and symmetric stretching vibrations of COO$^-$ related to citrate, respectively [44,45]. In addition, the intensity of peaks assigned to –OH and COO$^-$ were both significantly decreased suggesting that the interlayer citrate was removed by decomposition during calcination.

3.1.2. Shaping principle and stretchable nanopores

In order to investigate the intercalation effect of citrate, XRD patterns of a series of products were shown in Fig. 3A. It was clearly that the sharp reflection peaks of MA was appeared at 11.73°, 23.52°, 34.94°, 39.52° and 47.03°, corresponding to the crystal planes of (003), (006), (012), (015) and (018), respectively [46,47]. Obviously, all the characteristic peaks relating to LDH reappeared for T3@MA, but the peak positions had migrated towards lower angles [48], where the reflection peaks related to (003) and (006) crystal planes transformed to 7.35° and 14.67°. Hereby, it implied a broadening of basal spacing, suggesting the intercalation of citrate into the layers of T3@MA. Specifically, the basal spacing of the (003) reflection of MA and T3@MA was 7.54 Å and 12.00 Å by calculation. In addition, the thickness of LDH metal layer was already known to be 4.8 Å [25,49]. The space occupied by citrate could be easily deduced to be 7.2 Å, which was in perfect agreement with the molecular size of citrate obtained from Chem 3D combined with Multiwfn as displayed in Fig. S1A-B. Therefore, it was implying that the arrangement of citrate in the LDH interlayer might be a monolayer state and perpendicular to the host layer shown in Fig. S1C. However, the
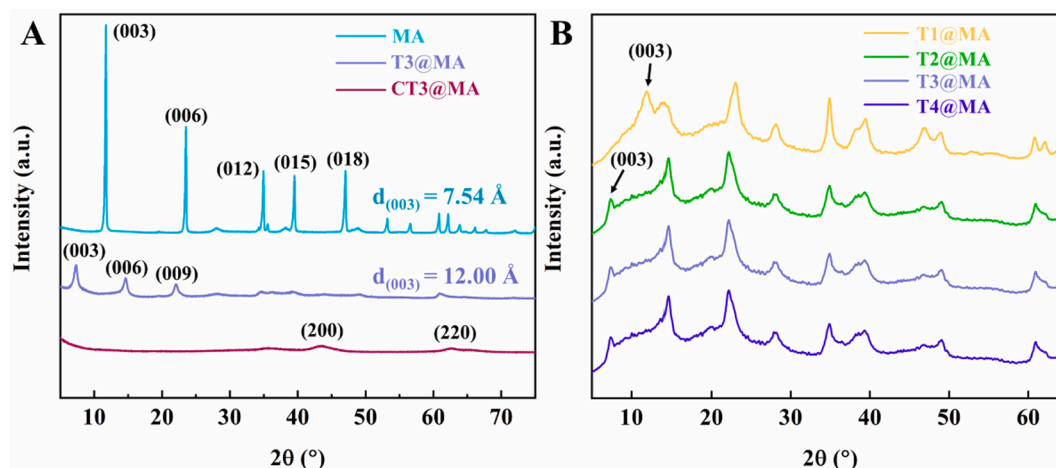

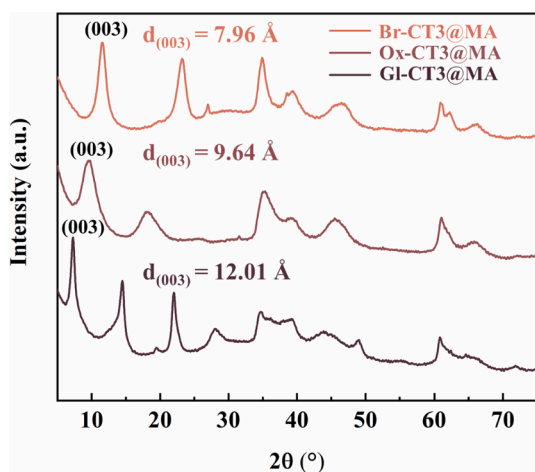**Fig 3.** The XRD patterns of MA, T1@MA, T2@MA, T3@MA, T4@MA and CT3@MA.

Fig. 4. The XRD patterns of CT3@MA adsorbed bromide (Br-CT3@MA), oxalate (Ox-CT3@MA) and gluconate (Gl-CT3@MA).

characteristic peaks of LDH all disappeared after calcination while the reflection peaks of 42.45° and 62.01° corresponding to the (200) and (220) lattice planes belonged to the crystalline phase of MgO for CT3@MA, indicating that T3@MA was subjected to violent dehydration and citrate decomposition to form CT3@MA in the course of pyrolysis [50].

Furthermore, XRD patterns of LDH synthesized in Fig. 3B by different TSC amount were also characterized for exploiting the role of citrate. Evidently, the peak attributed to the (003) crystal plane of T1@MA was at 11.71°, which was in accordance with that of MA. It was predicting that the citrate had not entered the interlayer, but the morphology of T1@MA was dramatically different from that of MA according to Fig. 1A-B. Nevertheless, the peak attributed to the (003) crystal plane of T2@MA shift to 7.35° indicating the intercalation of citric, similarly for T3@MA and T4@MA. At the same time, the shape of product developed towards a hierarchical spherical morphology assembled from small nanoplates. Hence, the forming mechanism could be inferred in conjunction with the morphological changes and the XRD patterns variations. When there was no citrate in the system, the concentration of free metal ions was high and active. Thus, the nucleation and growth rate of the monomer during the reaction was rapid, leading to the formation of large crystals and the product turn to large bulk and variable in size. And it was universally known that citrate was an extremely strong metal ion complexing agent. The citrate in the system would tend to catch metal ions, which leaded to a lower concentration of free Al^{3+}

and Mg^{2+} resulting in a lower rate of nucleation and crystallization of the LDH and then diminished the size and thickness of the product. Also, the surface energy of individual nanosheets was high from thermodynamic perspective and the optimum approach to reducing the surface energy of nanosheets was effective and ordered agglomeration [51,52]. Thus, the nanosheets became smaller as the citrate addition increased, and eventually the small-sized irregular flakes spontaneously self-assembled into stacks of completed spherical particles. In summary, citrate was inserted between the layers of LDH as a complexing agent and acted as a linker to facilitate the assembly of the flakes during the reaction. Analogously, citric had been employed extensively as a crystallization control or bridging agent in the synthesis of nanoscale metal compounds in a broad variety of shapes and structure [53–56].

With a view to exploit the memory effect and stretchable nanopores of CT3@MA, adsorption experiments with different sized anions including bromide, oxalate and gluconate were carried out, of which the XRD results were shown in Fig. 4. As we known, the ionic radius of Br (I) was 1.96 Å. In addition, the size and molecule structure of oxalate and gluconate were displayed in Fig S2. Apparently, some typical peaks similar to MA or T3@MA appeared in their XRD patterns treated by different anion solutions, which meet that the anions were trapped in the layers of CT3@MA. Furthermore, it was noting that the reflection peaks related to (003) crystal plane of Br-CT3@MA, Ox-CT3@MA and Gl-CT3@MA were 11.10°, 9.15° and 7.35°, respectively. And the basal spacing of the (003) reflection of them were 7.96 Å, 9.64 Å and 12.01 Å by calculation. Thus, the space occupied by bromide, oxalate and gluconate also could be deduced to be 3.16 Å, 4.84 Å and 7.21 Å respectively, which were all slightly smaller than their molecular size which could be attributed to the insertion into the layers at an angle to the crystal plane. Therefore, the insertion of various anions allowed for different crystal spacing indicating that CT3@MA had adaptable and stretchable nanopores.

3.1.3. N_2 adsorption–desorption

N_2 adsorption–desorption isotherms would reveal the porosity of the product rely on the obtained specific surface area and pore size, as shown in Fig. 5. Theoretically, the specific surface area of the hierarchical flower-like spheres was expected to be much higher than that of the micro-sheet alone, and would increase further after calcination. In Fig. 5A, the isotherms of MA, T3@MA and CT3@MA could be categorized as type IV isotherm indicating that the sample contained mesopores [57]. In addition, the hysteresis loop as type H3 was obviously shown in the isotherms of T3@MA and CT3@MA owing to the aggregation and stack of nanoplates [35]. From Fig. 5B, it could be concluded that T3@MA had more pores concentrated below 10 nm compared to MA, but also possessed larger pores (20–40 nm) due to the stacking of
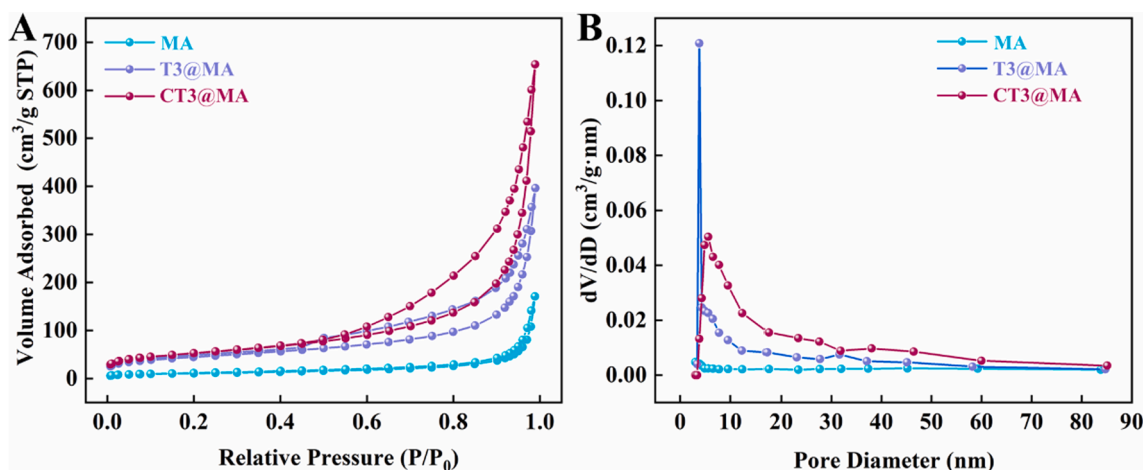

Fig. 5. N_2 adsorption–desorption isotherms (A) and pore size distribution (B) of MA, T3@MA and CT3@MA.

Table 2
Specific surface area (S$_{BET}$), total pore volume (V$_{tot}$) and average pore size (D$_{ave}$) of MA, T3@MA and CT3@MA.

Sample	S$_{BET}$ (m^2/g)	V$_{tot}$ (cm^3/g)	D$_{ave}$ (nm)
MA	37.7	0.260	3.408
T3@MA	158.6	0.613	3.827
CT3@MA	187.3	1.011	5.642

nanoplates. Moreover, CT3@MA had an increased pore size and a wider distribution. And the detailed data were listed in Table 2. The specific surface area of T3@MA was four times larger than that of MA and hold an enhanced average pore size and total pore volume. Furthermore, the specific surface area, average pore size and total pore volume of CT3@MA was also enlarged due to the removal of the majority of interlayer water and citrate by calcination. Therefore, CT3@MA was expected to hold an abundance of adsorption sites for toxins.

3.2. Adsorption isotherms and kinetics

LDO had a higher specific surface area and anion complexation capacity compared with LDH, so that CT3@MA would be capable of capturing HA or IS. For the purpose of predicting the maximum adsorption capacity and investigating the potential interaction between PBUTs and CT3@MA, the adsorption isotherm models such as Langmuir and Freundlich were employed to analyze the adsorption experiment data based on the relationship between the adsorption capacity and the equilibrium concentration of adsorbate. And the appropriate model was determined by the correlation coefficient (R^2) of the fitting equation. For the Langmuir model, there was an assumption that only a limited number of adsorption sites could capture the adsorbate. And the adsorption process only occurred as mono-layer, so that only one molecule of adsorbate was attached to each active site. Hence, once all the adsorption sites were occupied, the adsorbent would be unable to take up the adsorbate resulting in a saturated adsorption capacity. Conversely, the Freundlich model posited that as the concentration of adsorbate increased, the adsorbent surface allowed the adsorbate to be trapped by multi-layer adsorption, which was widely used to account for heterogeneous systems.

The effect of initial PBUTs concentration on the equilibrium adsorption capacity was shown in Fig. 6. Normally, the uptake of both HA or IS by CT3@MA increased significantly with increasing initial concentration of them. After a certain concentration was reached, the curve was often gently flattened to a plateau. From Fig. 6A, the equilibrium adsorption capacity of CT3@MA for HA and IS was 119.8 mg/g

Table 3
Langmuir and Freundlich constants for the adsorption of IS and HA.

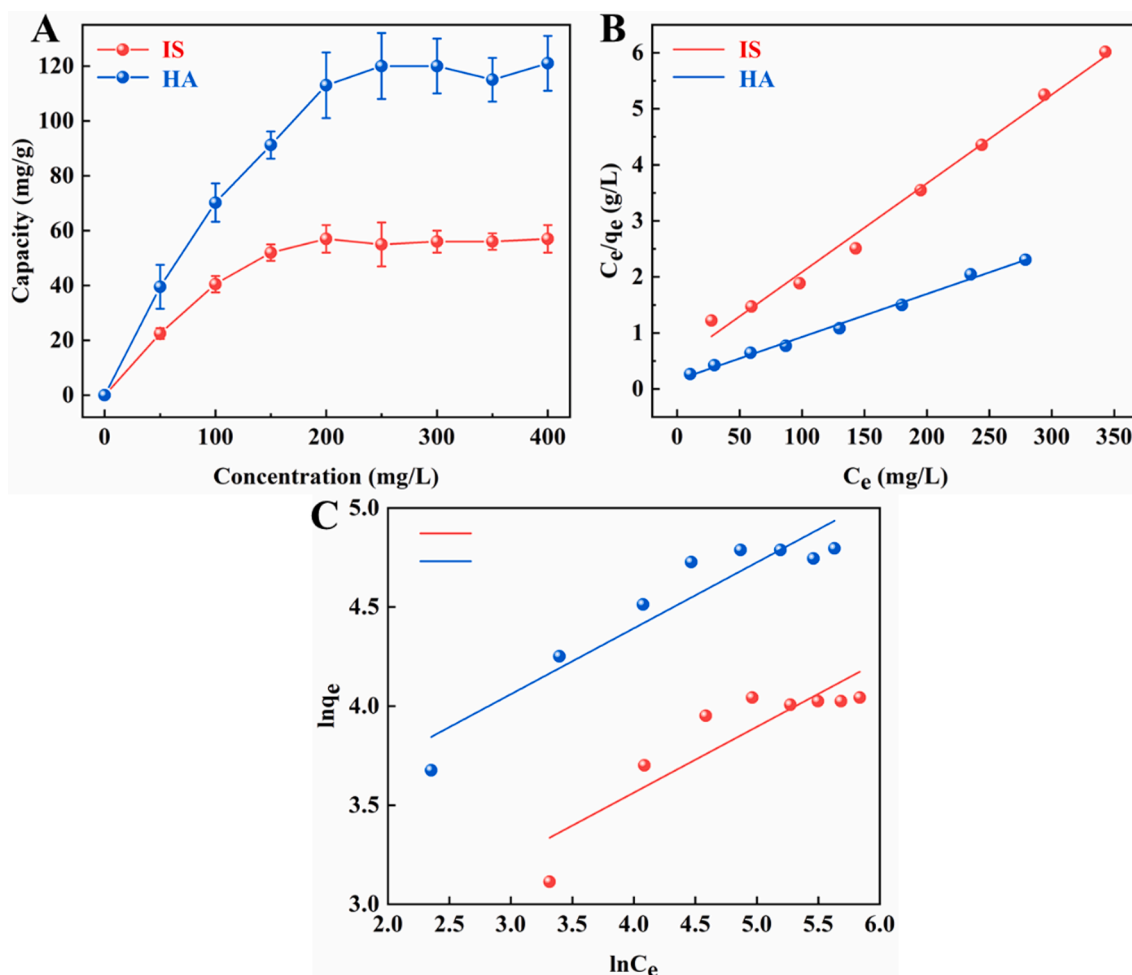| Adsorbates	Langmuir constants			Freundlich constants		
	q$_0$ (mg/g)	B (L/mg)	R^2	K$_F$ (mg/g)	n	R^2
IS	63.1	0.031	0.9899	9.3	3.01	0.7575
HA	129.8	0.048	0.9941	21.3	3.00	0.8701

Fig. 6. (A) Effect of initial concentration on the adsorption capacity of the CT3@MA for IS and HA. Adsorption isotherms of IS and HA depending on the Langmuir equation (B) and the Freundlich equation (C).

Table 4
The adsorption capacity of other adsorbents.

	Adsorbents	Capacity (mg/g)	
		HA	IS
Other works	CMK-3 (mesoporous carbon) [58]	12.2	3.2
	Norit (activated charcoal) [58]	12.6	3.7
	PES–zeolite composite membrane [59]	\	0.55
	rGO aerogel [13]	\	69.4
	poly-cyclodextrins [16]	\	45
This work	CT3@MA	129.8	63.1

and 57.5 mg/g, corresponding to equilibrium concentration of 250 mg/L and 200 mg/L, respectively. As illustrated in Fig. 6B-C, the adsorption curves were more closely aligned to the Langmuir fitting trend than that to Freundlich for both HA and IS. The parameters of the adsorption kinetics were presented in Table 3. Clearly, the adsorption process of HA or IS on CT3@MA was better described by the Langmuir model, indicating that the adsorption process was a mono-layer adsorption procedure on the homogeneous adsorbent. And the maximum adsorption capacity of HA and IS was up to 129.8 mg/g and 63.1 mg/g, respectively. Compared to conventional carbon materials and some adsorbents used in dialysate shown in Table 4, such impressive adsorption capacity indicated that CT3@MA would be utilized effectively for removing PBUTs.

To evaluate the adsorption rates of HA or IS on CT3@MA, the toxin adsorption experiments were carried out over a time range of 10 min to

300 min, both at an initial concentration of 300 mg/L. As shown in Fig. 7A, the adsorption capacity increased rapidly within the first 1 h, at which moment approximately 90 % of the adsorption capacity was accomplished because of the abundance of vacant adsorption sites in the initial phase. After that, the adsorption process continued in a slow growth period due to the reduction of the available adsorption sites until the plateau was established, which represented the completion of the adsorption. And the adsorption procedure reached equilibrium within 4 h, which exactly matched the treatment duration of clinical hemodialysis. In addition, the pseudo-first-order kinetic model and pseudo-second-order kinetic model were deployed to fitting experimental data to investigate further the adsorption process. Likewise, the best applicable model was determined by the correlation coefficient (R^2) of the two models. The kinetic fitting plots were depicted in Fig. 7B-C and the parameters were available in Table. 5. It was clear that the R^2 of the curves fitted with the pseudo-second-order kinetic model were much

Table 5
Adsorption kinetic parameters for the adsorption of IS and HA.

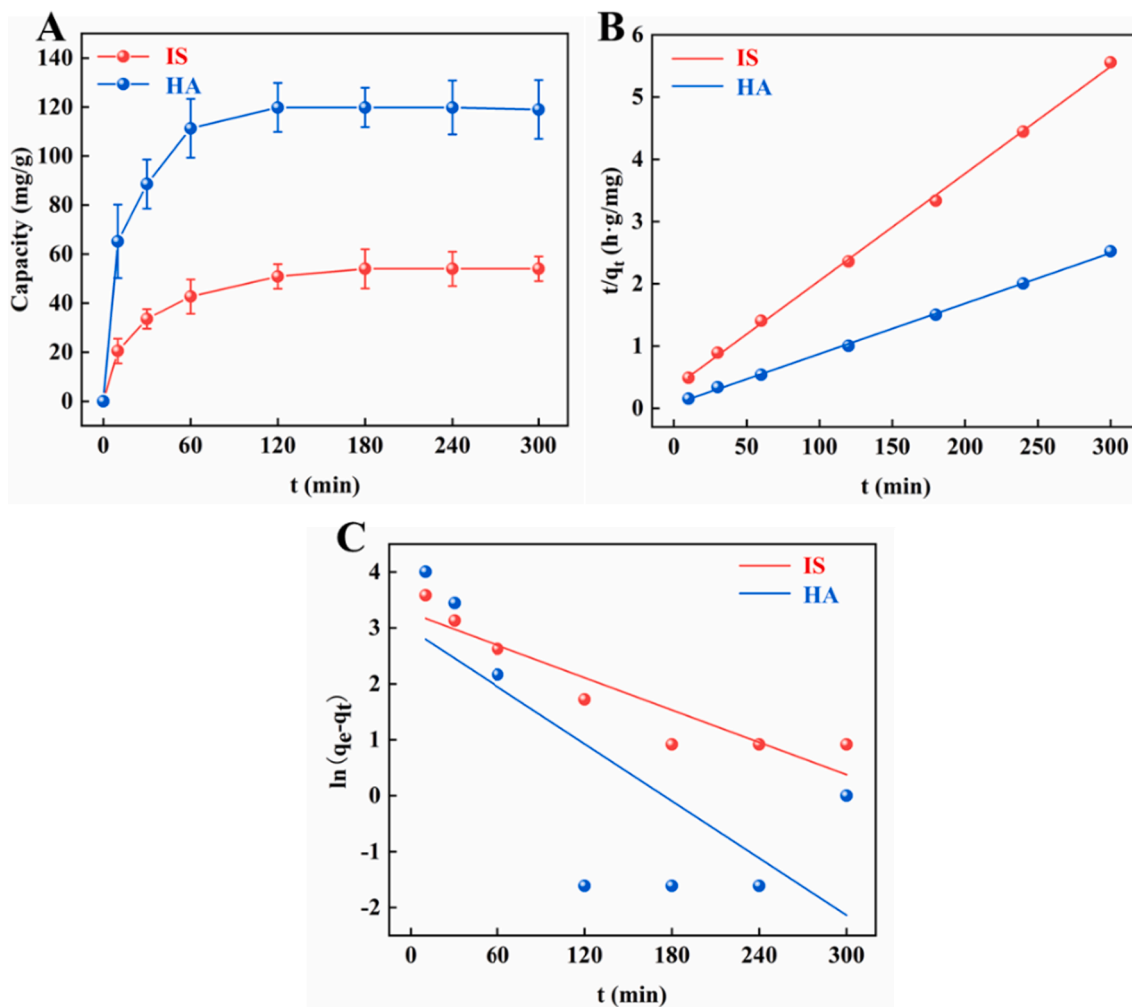| Adsorbates	Pseudo-first-order model			Pseudo-second-order model		
	q_e (mg/g)	K_1 (1/h)	R^2	q_e (mg/g)	K_2 ((g/(mg·h))	R^2
IS	26.2	0.0096	0.8423	58.1	0.0043	0.9991
HA	19.4	0.0170	0.4819	123.4	0.0001	0.9989

Fig. 7. (A) Effect of contact time on the adsorption capacity of the capacity of the CT3@MA for IS and HA. Pseudo-second-order kinetic model (B) and Pseudo-first-order kinetic model (C) for the adsorption process.
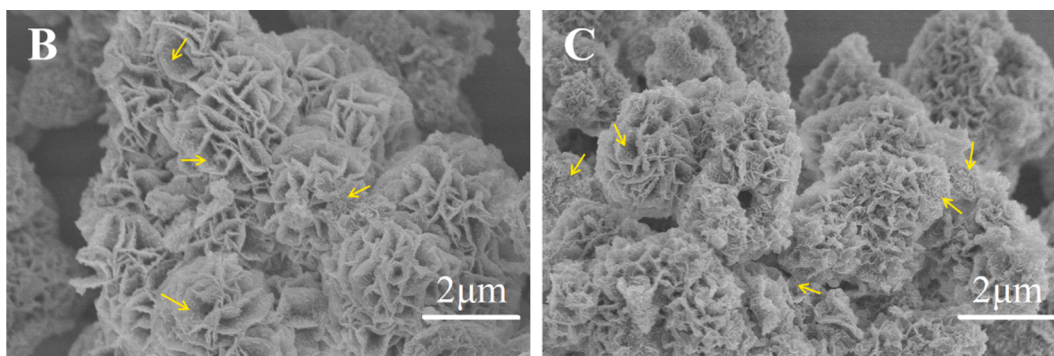
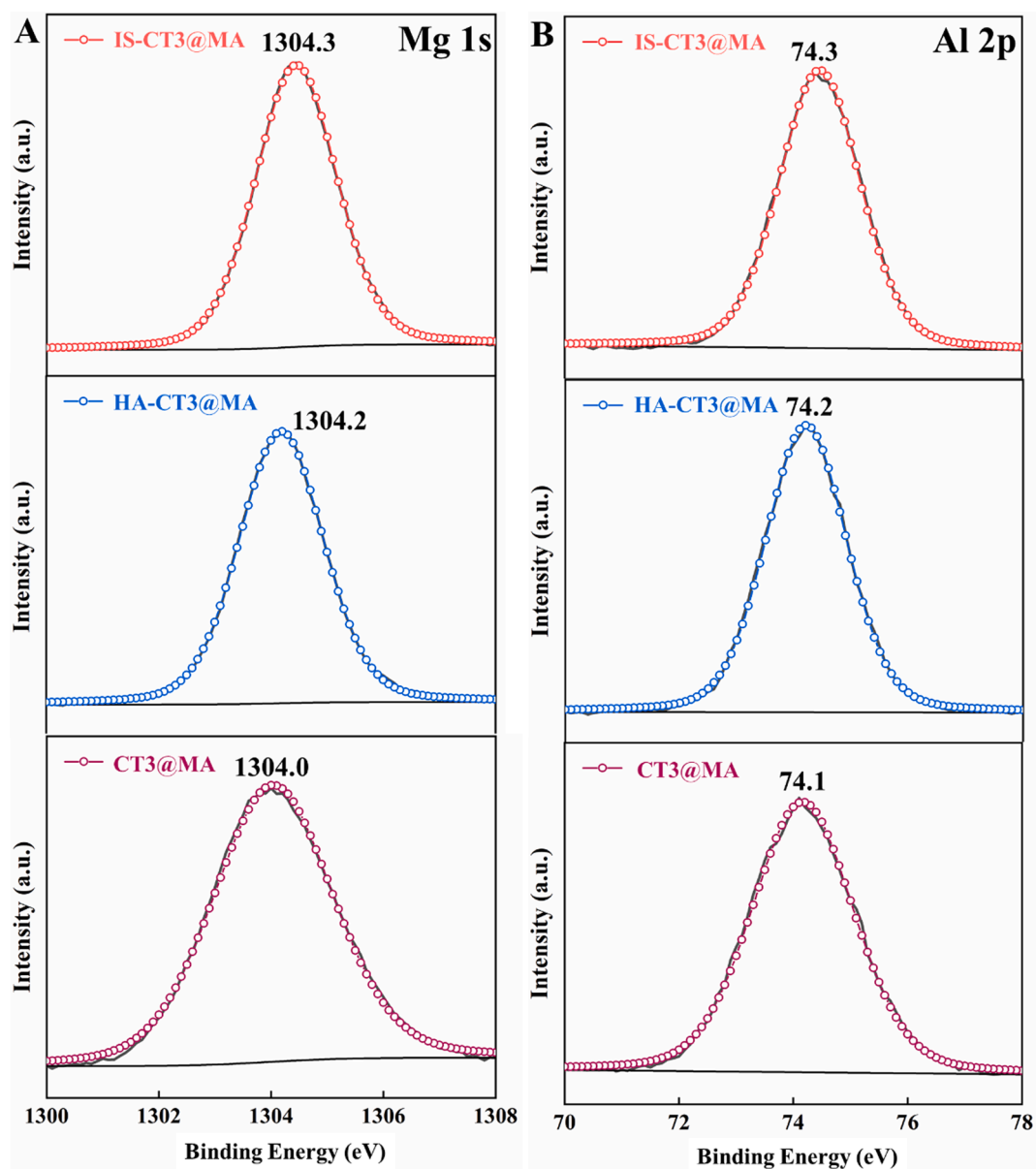**Fig. 8.** The SEM image of IS-CT3@MA (A) and HA-CT3@MA (B).

Fig. 9. The Mg 1s (A) and Al 2p (B) spectrum of CT3@MA, IS-CT3@MA and HA-CT3@MA.

higher than that fitted with the pseudo-first-order kinetic model for HA and IS. As expected, the fitted equilibrium adsorption capacity based on pseudo-second-order kinetic model (123.4 mg/g and 58.1 mg/g) was much closer to real experimental data (119.8 mg/g and 57.5 mg/g) than that on pseudo-first-order kinetic mode (19.4 mg/g and 26.2 mg/g), which implied that the adsorption of HA and IS was a classical chemical
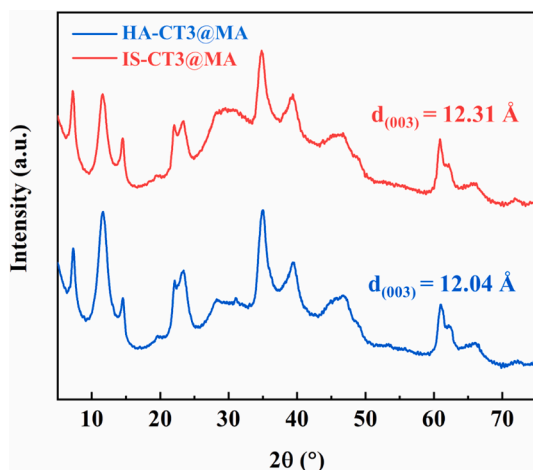
Fig. 10. The XRD patterns of IS-CT3@MA (A) and HA-CT3@MA (B).

interaction process. And the adsorption mechanism would be discussed in detail later.

According to our previous work [9,18], we had successfully reduced the volume of the dialysate to one tenth of its original volume by introducing toxin adsorbent into the dialysate. Obviously, small mass adsorbent (2 g) was able to replace large volume dialysate (1800 ml) while the toxin (creatinine) clearance remained at a high level (63 %), which illustrated the feasibility of lightweight hemodialysis and the importance of the adsorbent in the whole process [18]. For PBUTs, we had similarly performed rGO aerogel blocks as adsorbents into the dialysate to achieve efficient removal of IS with limited amounts of dialysate (200 ml) during the hemodialysis, of which the toxin clearance was increased from 36.5 % to 51.8 % with the assistance of adsorbents [13]. In this study, CT3@MA not only exhibited the maximum adsorption capacity (63.1 mg/g) for IS comparable to that of rGO aerogel (69.4 mg/g) and reached adsorption equilibrium (3 h) faster than rGO aerogel (4 h) [13], but also possessed a high adsorption capacity for HA (129.8 mg/g) and the adsorption equilibrium time was only 2 h. Therefore, the CT3@MA as an adsorbent towards PBUTs provided great adsorption

capacity and fast adsorption rate, which would definitely perform more effective removal of toxins in the same way indicating that it had great potential to be employed in family hemodialysis equipment.

3.3. Adsorption mechanism

In attempt to elucidate the mechanism of adsorption of PBUTs in detail, CT3@MA was characterized and analyzed by FE-SEM, XPS and XRD before and after adsorption. And samples after adsorption of HA and IS were labelled as HA-CT3@MA and IS-CT3@MA, respectively. On the one hand, the large specific surface area of CT3@MA inevitably provided abundant active sites for toxin adsorption. On the other hand, the extensive pore structure formed by the stacking of nanoplates also had a certain physical binding effect on toxins. In Fig. 8A-B, it was clear that the flower-like morphology of the nanoplates stacks remained after the adsorption of the PUBTs, proving the good stability of the LDO. However, the surface of the nanoplate showed abundant tiny folds, which may be the morphology formed by the micro-crystallization of HA or IS.

The XPS survey spectrums of samples were shown in Fig. S3 and Fig. 9. As seen from Fig. S3A, in contrast to CT3@MA, a few new elements of N and S appeared after adsorption. In addition, As shown in Fig. S3B-D, The peak with the binding energy 399.5 eV was attributed to N—C while the peaks with the binding energy 168.3 eV and 169.3 eV were attributed to S 2p3/2 and S 2p1/2 respectively from -SO$_3$ [60]. And in Fig. 9, it could be seen that the peak at 1304.0 eV and 74.1 eV were assigned to Mg-O and Al-O consistent with the formation of Mg and Al bimetallic oxides [61,62], which also demonstrate MgAl LDO was successfully prepared. Moreover, the peaks of Mg-O and Al-O in IS-CT3@MA and HA-CT3@MA were slightly shifted to the high binding energy indicating that there was electrostatic interaction of the PBUTs with the bimetallic oxides due to anisotropic charges. This provided ample evidence for the adsorption of PBUTs on CT3@MA.

Moreover, LDO was capable of incorporating anions into their layers to re-generate LDH structures through the so-called memory effect with stretchable nanopores. As shown in Fig. 10, it was found that the layered structure of the LDH material was reconstructed, which could be deduced from the proximity of its XRD pattern to MA and CT3@MA. Interestingly, the peak attributed to (0 0 3) plane was at 7.33° and 7.17°
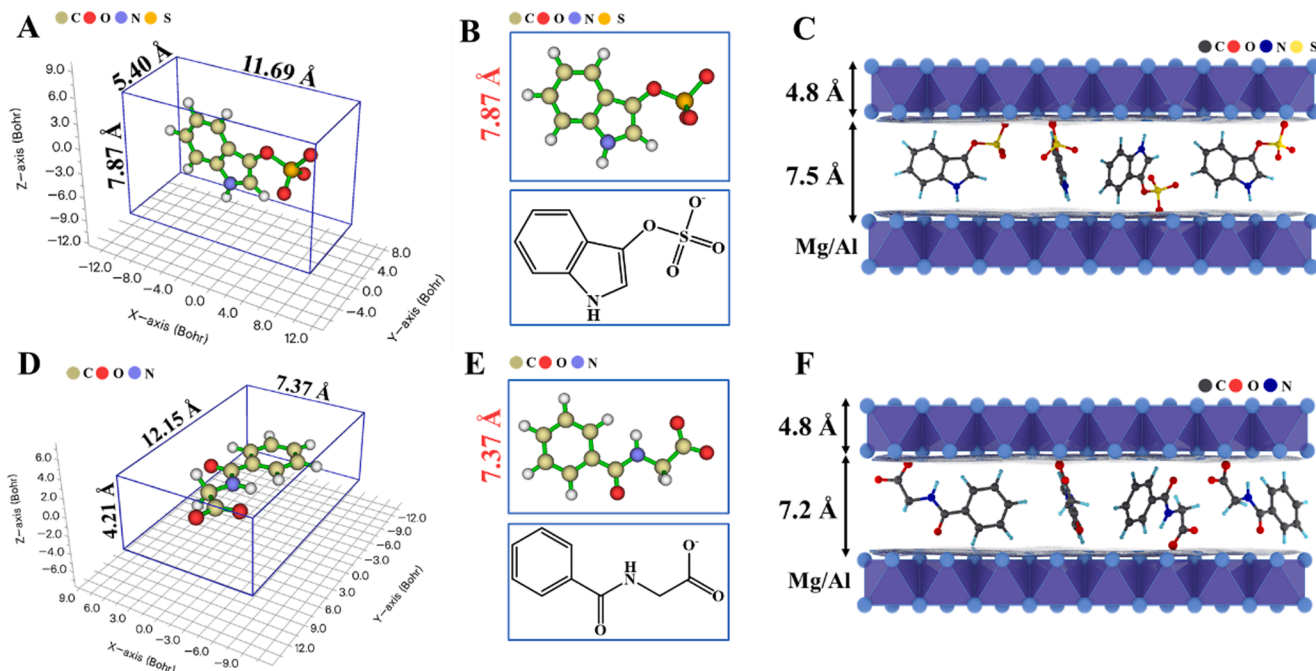

Fig. 11. The molecular structure, molecular size and intercalation effect of IS (A, B and C) and HA (D, E and F).

for HA-CT3@MA and IS-CT3@MA respectively, which demonstrated that the crystal plane spacing could be calculated to be 12.04 Å and 12.37 Å. Likewise, the space occupied by HA and IS could be easily deduced to be about 7.24 Å and 7.57 Å, respectively. Furthermore, the molecule size of HA and IS was shown in Fig. 11. By Chem 3D combined with Multiwfn, the dimensions on the plane of the benzene ring in the molecule were found to be 7.37 Å and 7.87 Å for HA and IS, which was close to the interlayer distances characterized by XRD. Therefore, the HA and IS was intercalated between the layers at a small angle to the normal of the metal layer shown in Fig. 11C and 11F. The foregoing illustrated the intercalation effect of PUBTs in CT3@MA to achieve efficient adsorption.

4. Conclusion

In this work, we had prepared flower-like spherical MgAl LDO with delicate hierarchical structure and stretchable nanopores using citrate as a morphological control agent through a facile one-pot hydrothermal method followed by calcination treatment, providing a wealth of active sites for adsorption due to the ultrahigh specific surface area. Moreover, taking advantage of the unique memory effect and stretchable nanopores of LDO, the maximum adsorption capacity of HA and IS was 129.8 mg/g and 63.1 mg/g respectively relying on electrostatic interaction to capture toxins by surface adsorption and interlayer intercalation. In summary, the design and application of such LDO not only provided a new reference for the construction of nano-materials with hierarchical structures, but also potentially promised to provide new options for the development of family hemodialysis devices and portable artificial kidneys.

CRediT authorship contribution statement

Siping Ding: Conceptualization, Investigation, Data curation, Writing – original draft, Visualization, Validation. **Dong Wang:** Investigation, Resources. **Xuefen Wang:** Methodology, Writing – review & editing, Supervision, Project administration, Funding acquisition.

Declaration of Competing Interest

The authors declare that they have no known competing financial interests or personal relationships that could have appeared to influence the work reported in this paper.

Data availability

Data will be made available on request.

Acknowledgements

Appendix A. Supplementary material

Supplementary data to this article can be found online at https://doi.org/10.1016/j.seppur.2022.122033.

References

[1] M.K. Van Gelder, J.A.W. Jong, L. Folkertsma, Y. Guo, C. Bluchel, M.C. Verhaar, M. Odijk, C.F. Van Nostrum, W.E. Hennink, K.G.F. Gerritsen, Urea removal strategies for dialysate regeneration in a wearable artificial kidney, Biomaterials 234 (2020) 119735.

[2] V.A. Luyckx, Z. Al-Aly, A.K. Bello, E. Bellorin-Font, R.G. Carlini, J. Fabian, G. Garcia-Garcia, A. Iyengar, M. Sekkarie, W. van Biesen, I. Ulasi, K. Yeates, J. Stanifer, Sustainable development goals relevant to kidney health: an update on progress, Nat. Rev. Nephrol. 17 (1) (2021) 15–32.

[3] Y. Cheng, R. Luo, K. Wang, M. Zhang, Z. Wang, L. Dong, J. Li, Y. Yao, S. Ge, G. Xu, Kidney disease is associated with in-hospital death of patients with COVID-19, Kidney Int. 97 (5) (2020) 829–838.

[4] H. Zhao, J. Huang, L. Miao, Y. Yang, Z. Xiao, Q. Chen, Q. Huang, K. Ai, Toward urease-free wearable artificial kidney: Widened interlayer spacing MoS$_2$ nanosheets with highly effective adsorption for uremic toxins, Chem. Eng. J. 438 (2022), 135583.

[5] J. Jansen, J. Jankowski, P.R. Gajjala, J.F.M. Wetzels, R. Masereeuw, Disposition and clinical implications of protein-bound uremic toxins, Clin. Sci. 131 (2017) 1631–1647.

[6] M. Sternkopf, S. Thoroe-Boveleth, T. Beck, K. Oleschko, A. Erlenkotter, U. Tschulena, S. Steppan, T. Speer, C. Goettsch, V. Jankowski, J. Jankowski, H. Noels, E. European Uremic Toxin Work Group, A bifunctional adsorber particle for the removal of hydrophobic uremic toxins from whole blood of renal failure patients, Toxins 11 (2019) 389.

[7] X. Yu, L. Shen, Y. Zhu, X. Li, Y. Yang, X. Wang, M. Zhu, B.S. Hsiao, High performance thin-film nanofibrous composite hemodialysis membranes with efficient middle-molecule uremic toxin removal, J. Membr. Sci. 523 (2017) 173–184.

[8] V. Gura, M.B. Rivara, S. Bieber, R. Munshi, N.C. Smith, L. Linke, J. Kundzins, M. Beizai, C. Ezon, L. Kessler, J. Himmelfarb, A wearable artificial kidney for patients with end-stage renal disease, Jci. Insight. 1 (2016) e86397.

[9] S. Ding, T. Zhang, P. Li, X. Wang, Dialysis/adsorption bifunctional thin-film nanofibrous composite membrane for creatinine clearance in portable artificial kidney, J. Membr. Sci. 636 (2021), 119550.

[10] M.L. Mendu, J.C. Divino-Filho, R. Vanholder, S. Mitra, S.J. Davies, V. Jha, K. C. Damron, D. Gallego, M. Seger, C. International home dialysis roundtable steering, expanding utilization of home dialysis: an action agenda from the first international home dialysis roundtable, Kidney Med. 3 (2021) 635–643.

[11] M. Khatri, S. Islam, P. Dutka, J. Carson, J. Drakakis, L. Imbriano, I. Jawaid, T. Mehta, N. Miyawaki, E. Wu, S. Yang, N. Ali, J. Divers, C. Grant, N. Masani, COVID-19 antibodies and outcomes among outpatient maintenance hemodialysis patients, Kidney360 2 (2) (2021) 263–269.

[12] K. Tharpa, P.S. Mahabala, C.S. Gurunath, J. Jose, S. Tantry, R. Choorikkat, D. Tymoshenko, H. de Brouwer, A. Kumar, New chemistry supporting portable solutions for end-stage renal disease dialysis treatment, J. Artif. Organs. 23 (1) (2020) 47–53.

[13] Y. Jin, S. Ding, P. Li, X. Wang, Coordination of thin-film nanofibrous composite dialysis membrane and reduced graphene oxide aerogel adsorbents for elimination of indoxyl sulfate, Chin. J. Chem. Eng. 49 (2022) 111–121.

[14] D. Bergé-Lefranc, F. Chaspoul, R. Calaf, P. Charpiot, P. Brunet, P. Gallice, Binding of p-Cresylsulfate and p-Cresol to human serum albumin studied by microcalorimetry, J. Phys. Chem. B 114 (4) (2010) 1661–1665.

[15] M.S.L. Tijink, M. Wester, G. Glorieux, K.G.F. Gerritsen, J. Sun, P.C. Swart, Z. Borneman, M. Wessling, R. Vanholder, J.A. Joles, D. Stamatialis, Mixed matrix hollow fiber membranes for removal of protein-bound toxins from human plasma, Biomaterials 34 (32) (2013) 7819–7828.

[16] J. Li, L. Han, S. Liu, S. He, Y. Cao, J. Xie, L. Jia, Removal of indoxyl sulfate by water-soluble poly-cyclodextrins in dialysis, Colloids Surf. B 164 (2018) 406–413.

[17] J. Li, L. Han, J. Xie, S. Liu, L. Jia, Multi-sites polycyclodextrin adsorbents for removal of protein-bound uremic toxins combining with hemodialysis, Carbohydr. Polym. 247 (2020), 116665.

[18] S. Ding, P. Li, T. Zhang, X. Wang, Coordination of copper ion crosslinked composite beads with enhanced toxins adsorption and thin-film nanofibrous composite membrane for realizing the lightweight hemodialysis, Adv. Fiber Mater. 4 (3) (2022) 556–570.

[19] X. Yuan, Y. Wang, J. Wang, C. Zhou, Q. Tang, X. Rao, Calcined graphene/MgAl-layered double hydroxides for enhanced Cr(VI) removal, Chem. Eng. J. 221 (2013) 204–213.

[20] J. Poonoosamy, F. Brandt, M. Stekiel, P. Kegler, M. Klinkenberg, B. Winkler, V. Vinograd, D. Bosbach, G. Deissmann, Zr-containing layered double hydroxides: synthesis, characterization, and evaluation of thermodynamic properties, Appl. Clay. Sci. 151 (2018) 54–65.

[21] P. Li, P.-P. Huang, F.-F. Wei, Y.-B. Sun, C.-Y. Cao, W.-G. Song, Monodispersed Pd clusters generated in situ by their own reductive support for high activity and stability in cross-coupling reactions, J. Mater. Chem. A 2 (2014) 12739.

[22] Q. Song, W. Liu, C.D. Bohn, R.N. Harper, E. Sivaniah, S.A. Scott, J.S. Dennis, A high performance oxygen storage material for chemical looping processes with CO$_2$ capture, Energy Environ. Sci. 6 (2013) 288.

[23] F. Song, X. Hu, Exfoliation of layered double hydroxides for enhanced oxygen evolution catalysis, Nat. Commun. 5 (2014) 4477.

[24] P. Li, W. Liu, J.S. Dennis, H.C. Zeng, Ultrafine alloy nanoparticles converted from 2d intercalated coordination polymers for catalytic application, Adv. Funct. Mater. 26 (31) (2016) 5658–5668.

[25] X. Qiu, K. Sasaki, T. Hirajima, K. Ideta, J. Miyawaki, One-step synthesis of layered double hydroxide-intercalated gluconate for removal of borate, Sep. Purif. Technol. 123 (2014) 114–123.

[26] P. Zhang, T. He, P. Li, X. Zeng, Y. Huang, New insight into the hierarchical microsphere evolution of organic three-dimensional layer double hydroxide: the key role of the surfactant template, Langmuir 35 (2019) 13562–13569.

[27] L. Chen, Q. Tu, X. Yang, X. Hu, X. Sun, H. Li, MgAl layered double hydroxides intercalated with EDTA Cu II recovery and mechanism, ChemistrySelect 5 (36) (2020) 11299–11304.

[28] J. Zhang, X. Xie, C. Li, H. Wang, L. Wang, The role of soft colloidal templates in the shape evolution of flower-like MgAl-LDH hierarchical microstructures, Rsc Adv. 5 (38) (2015) 29757–29765.

[29] S.-M. Xu, Q.-C. Zhu, J. Long, H.-H. Wang, X.-F. Xie, K.-X. Wang, J.-S. Chen, Low-overpotential Li-O₂ batteries based on TFSI intercalated Co-Ti layered double oxides, Adv. Funct. Mater. 26 (9) (2016) 1365–1374.

[30] Y. Zou, X. Wang, F. Wu, S. Yu, Y. Hu, W. Song, Y. Liu, H. Wang, T. Hayat, X. Wang, Controllable synthesis of Ca-Mg-Al layered double hydroxides and calcined layered double oxides for the efficient removal of U(VI) from wastewater solutions, ACS Sustain. Chem. Eng. 5 (1) (2017) 1173–1185.

[31] X. Zhang, J. Shen, Y. Ma, L. Liu, R. Meng, J. Yao, Highly efficient adsorption and recycle of phosphate from wastewater using flower-like layered double oxides and their potential as synergistic flame retardants, J. Colloid. Interf. Sci. 562 (2020) 578–588.

[32] J. Wang, B. Huang, Z. Mao, Y. Wang, Study on adsorption properties of calcined Mg-Al hydrotalcite for sulfate ion and chloride ion in cement paste, Materials 14 (2021) 994.

[33] P. Kowalik, M. Konkol, M. Kondracka, W. Próchniak, R. Bicki, P. Wiercioch, Memory effect of the CuZnAl-LDH derived catalyst precursor—In situ XRD studies, Appl. Catal. A-Gen. 464 (2013) 339–347.

[34] Y. Guo, Z. Zhu, Y. Qiu, J. Zhao, Enhanced adsorption of acid brown 14 dye on calcined Mg/Fe layered double hydroxide with memory effect, Chem. Eng. J. 219 (2013) 69–77.

[35] Y. Zheng, B. Cheng, W. You, J. Yu, W. Ho, 3D hierarchical graphene oxide-NiFe LDH composite with enhanced adsorption affinity to Congo red, methyl orange and Cr(VI) ions, J. Hazard. Mater. 369 (2019) 214–225.

[36] X. Guo, Y. Shang, X. Liang, Z. Diao, G. Song, D. Chen, S. Wang, L. Kong, A comparison of Ni-Co layered double oxides with memory effect on recovering U (VI) from wastewater to hydroxides, Chem. Eng. J. 446 (2022), 137220.

[37] C. Lei, X. Zhu, B. Zhu, C. Jiang, Y. Le, J. Yu, Superb adsorption capacity of hierarchical calcined Ni/Mg/Al layered double hydroxides for Congo red and Cr (VI) ions, J. Hazard. Mater. 321 (2017) 801–811.

[38] Z. Zhu, P. Wu, G. Liu, X. He, B. Qi, G. Zeng, W. Wang, Y. Sun, F. Cui, Ultrahigh adsorption capacity of anionic dyes with sharp selectivity through the cationic charged hybrid nanofibrous membranes, Chem. Eng. J. 313 (2017) 957–966.

[39] Y. Feng, Y. Wang, Y. Wang, X.F. Zhang, J. Yao, In-situ gelation of sodium alginate supported on melamine sponge for efficient removal of copper ions, J. Colloid. Interf. Sci. 512 (2018) 7–13.

[40] T. Lu, F. Chen, Multiwfn: a multifunctional wavefunction analyzer, J. Comput. Chem. 33 (2012) 580–592.

[41] Y. Yu, J. Paul Chen, Key factors for optimum performance in phosphate removal from contaminated water by a Fe-Mg-La tri-metal composite sorbent, J. Colloid. Interf. Sci. 445 (2015) 303–311.

[42] Y. Qiao, Q. Li, H. Chi, M. Li, Y. Lv, S. Feng, R. Zhu, K. Li, Methyl blue adsorption properties and bacteriostatic activities of Mg-Al layer oxides via a facile preparation method, Appl. Clay. Sci. 163 (2018) 119–128.

[43] H. Ji, W. Wu, F. Li, X. Yu, J. Fu, L. Jia, Enhanced adsorption of bromate from aqueous solutions on ordered mesoporous Mg-Al layered double hydroxides (LDHs), J. Hazard. Mater. 334 (2017) 212–222.

[44] Z. Xu, Q. Zhao, T. Liu, L. Wang, S. Bian, Uniform and well-dispersed YbVO₄ hierarchical nanoarchitectures: synthesis and luminescence properties, J. Nanosci. Nanotechno. 13 (2013) 344–350.

[45] L. Zhang, L. Fu, X. Yang, Z. Fu, X. Qi, Z. Wu, Controlled synthesis and tunable luminescence of uniform YPO₄·0.8H₂O and YPO₄·0.8H₂O : Tb³⁺/Eu³⁺ nanocrystals by a facile approach, J. Mater. Chem. C 2 (2014) 9149–9158.

[46] Z. Xu, G. Lu, Hydrothermal synthesis of layered double hydroxides (LDHs) from mixed MgO and Al₂O₃: LDH formation mechanism, Chem. Mater. 17 (2005) 1055–1062.

[47] T. Wen, X. Wu, X. Tan, X. Wang, A. Xu, One-pot synthesis of water-swellable Mg-Al layered double hydroxides and graphene oxide nanocomposites for efficient removal of As(V) from aqueous solutions, ACS Appl. Mater. Inter. 5 (8) (2013) 3304–3311.

[48] Q. Li, R.J. Kirkpatrick, Organic anions in layered double hydroxides: an experimental investigation of citrate hydrotalcite, Am. Mineral. 92 (2007) 397–402.

[49] A.G.K.P. Padma Kumar, R. James Kirkpatrick, Hydration, swelling, interlayer structure, and hydrogen bonding in organolayered double hydroxides: Insights from molecular dynamics simulation of citrate-intercalated hydrotalcite, J. Phys. Chem. B 110 (2006) 3841–3844.

[50] P. Li, Y. Yu, P.-P. Huang, H. Liu, C.-Y. Cao, W.-G. Song, Core–shell structured MgAl-LDO@Al-MS hexagonal nanocomposite: an all inorganic acid–base bifunctional nanoreactor for one-pot cascade reactions, J. Mater. Chem. A 2 (2014) 339–344.

[51] L. Yuan, Z. Yang, F. Cui, Y. Rong, Q. Su, H. Chen, J. Wu, L. Deng, Flower-like Zn-Al-In layered double oxides synthesized by a facile hydrothermal method as ultra-high cycle stability anodic for zinc-nickel battery, J. Alloys Compd. 863 (2021), 158574.

[52] Y. Bao, C. Wang, J. Ma, Trisodium citrate as bridging and suppressing agent to control synthesis of ZnO hollow hierarchical microspheres and their photocatalytic properties, Ceram. Int. 42 (1) (2016) 1746–1755.

[53] S. Wang, G. Qiao, X. Chen, X. Wang, H. Cui, Synthesis of ZnO hollow microspheres and analysis of their gas sensing properties for n-butanol, Crystals 10 (2020) 1010.

[54] M.B. Zakaria, E.-Z. Ebeid, M.M. Abdel-Galeil, T. Chikyow, Cyanide bridged coordination polymer nanoflakes thermally derived Ni3C and fcc-Ni nanoparticles for electrocatalysts, New J. Chem. 41 (24) (2017) 14890–14897.

[55] M.B. Zakaria, M.S.A. Hossain, M.J.A. Shiddiky, M. Shahabuddin, E. Yanmaz, J. H. Kim, A.A. Belik, Y. Ide, M. Hu, S. Tominaka, Y. Yamauchi, Cyano-bridged trimetallic coordination polymer nanoparticles and their thermal decomposition into nanoporous spinel ferromagnetic oxides, Chemistry 22 (42) (2016) 15042–15048.

[56] S. Suwanboon, W. Somraksa, P. Amornpitoksuk, C. Randorn, Effect of trisodium citrate on the formation and structural, optical and photocatalytic properties of Sr-doped ZnO, J. Alloys Compd. 832 (2020) 154963.

[57] M. Thommes, K. Kaneko, A.V. Neimark, J.P. Olivier, F. Rodriguez-Reinoso, J. Rouquerol, K.S.W. Sing, Physisorption of gases, with special reference to the evaluation of surface area and pore size distribution (IUPAC Technical Report), Pure Appl. Chem. 87 (2015) 1051–1069.

[58] D. Pavlenko, D. Giasafaki, G. Charalambopoulou, E. van Geffen, K.G.F. Gerritsen, T. Steriotis, D. Stamatialis, Carbon adsorbents with dual porosity for efficient removal of uremic toxins and cytokines from human plasma, Sci. Rep. 7 (2017) 14914.

[59] L. Lu, J.T.W. Yeow, An adsorption study of indoxyl sulfate by zeolites and polyethersulfone–zeolite composite membranes, Mater. Des. 120 (2017) 328–335.

[60] N. Maiti, S. Thomas, A. Debnath, S. Kapoor, Raman and XPS study on the interaction of taurine with silver nanoparticles, Rsc Adv. 6 (61) (2016) 56406–56411.

[61] T. Hou, L. Yan, J. Li, Y. Yang, L. Shan, X. Meng, X. Li, Y. Zhao, Adsorption performance and mechanistic study of heavy metals by facile synthesized magnetic layered double oxide/carbon composite from spent adsorbent, Chem. Eng. J. 384 (2020), 123331.

[62] Y. Sun, W.-M. Yin, Y. Wang, N.-D. Zhao, X.-Y. Wang, J.-G. Zhang, Y.-R. Guo, S. Li, Q.-J. Pan, Fabrication of ultra-thin MgAl layered double oxide by cellulose templating and its immobilization effect toward heavy metal ions: cation-exchange and deposition mechanism, Chem. Eng. J. 427 (2022), 132017.